Laser ion acceleration via control of the near-critical density target

A. Yogo,[1] H. Daido,[1] S. V. Bulanov,[1] K. Nemoto,[2] Y. Oishi,[2] T. Nayuki,[2] T. Fujii,[2] K. Ogura,[1] S. Orimo,[1] A. Sagisaka,[1] J.-L. Ma,[1] T. Zh. Esirkepov,[1] M. Mori,[1] M. Nishiuchi,[1] A. S. Pirozhkov,[1] S. Nakamura,[3,*] A. Noda,[3] H. Nagatomo,[4] T. Kimura,[1] and T. Tajima[1]

[1]*Kansai Photon Science Institute, Japan Atomic Energy Agency (JAEA), Kyoto 619-0215, Japan*
[2]*Central Research Institute of Electric Power Industry (CRIEPI), Kanagawa 240-0196, Japan*
[3]*Institute for Chemical Research, Kyoto University, Kyoto 611-0011, Japan*
[4]*Institute of Laser Engineering, Osaka University, Osaka 565-0871, Japan*

(Received 30 July 2007; published 8 January 2008)

Duration-controlled amplified spontaneous emission with an intensity of 10^{13} W/cm^2 is used to convert a 7.5-μm-thick polyimide foil into a near-critical plasma, in which the *p*-polarized, 45-fs, 10^{19}-W/cm^2 laser pulse generates 3.8-MeV protons, emitted at some angle between the target normal and the laser propagation direction of 45°. Particle-in-cell simulations reveal that the efficient proton acceleration is due to the generation of a quasistatic magnetic field on the target rear side with magnetic pressure inducing and sustaining a charge separation electrostatic field.

DOI: 10.1103/PhysRevE.77.016401 PACS number(s): 52.38.Kd, 29.27.Fh

I. INTRODUCTION

Advances in the technology of ultraintense lasers are propelling studies of the laser-driven ion acceleration [1]. When a laser pulse with intensity well exceeding 10^{18} W/cm^2 irradiates a foil target, the laser-field-driven force accelerates electrons at the target surface up to relativistic velocity. A portion of the accelerated electrons passes through the target toward the rear side, resulting in generation of an electrostatic field, which accelerates ions at the target rear surface. The laser-target interaction can be complicated by the presence of an amplified spontaneous emission (ASE) pedestal at a leading edge of the high-intensity laser pulse. A nanosecond ASE pedestal with intensity of the order of 10^{12} W/cm^2 can heat the target causing its expansion and preplama formation. As shown in experiments [2], the formation of a plasma corona at a rear side of a relatively thick target can hamper ion acceleration. As shown in Ref. [3], in the framework of the target normal sheath acceleration (TNSA) mechanism [4], based on an ambipolar plasma expansion into vacuum [5], even a slight breakout of the rear surface may drastically decrease the ion energy. In addition, the ASE pedestal can generate a shock wave which propagates through the target, deforming its rear side, thus changing the spatial distribution of the ion-accelerating electric field [6–8]. For the acceleration regimes, discussed in the above-mentioned references, a "clean" laser pulse without ASE is desired for achieving higher-energy ions. Recently, plasma mirrors were demonstrated to efficiently suppress ASE, making it 10^{10}–10^{12} times lower in intensity than the main pulse (see [9]). This made possible proton generation with targets of nanometer thickness [10]. On the other hand, Matsukado *et al.* [11] observed protons accelerated from a thin-foil target, the laser-irradiated region of which was evaporated by the ASE pedestal with the formation of a near-critical density plasma profile [12]. Willingale *et al.* [13] demonstrated an efficient laser-driven ion acceleration with a gas-jet target.

In this paper, we use a nanosecond ASE pedestal as a tool for controlling the target parameters seen by the main (femtosecond) laser pulse. The ASE pedestal causes expansion of a thin-foil target, thus reducing the target density to the order of the plasma critical density. A high-intensity femtosecond laser pulse can penetrate this modified target, accelerating electrons. Their current, together with the return current of bulk electrons, form a long-living quasistatic magnetic field, which induces and sustains a charge separation electrostatic field at the rear side, providing the ion acceleration [11,14]. Changing the ASE duration, we modify the target by arranging an optimal absorption of the laser pulse energy, maximizing the ion energy [14,15]. The plasma density profile is measured using the interferometry and investigated with two-dimensional (2D) hydrodynamic (HD) simulations. The proton-energy spectra are observed using the online time-of-flight (TOF) spectrometers for a wide range of ASE durations. The features of the proton acceleration (maximum energy and emission direction) are explained with the help of 2D particle-in-cell (PIC) simulations.

II. EXPERIMENTAL SETUP

The experiment was performed with the Ti:sapphire laser system at CRIEPI [16,17]. The experimental setup is shown in Fig. 1. A *p*-polarized laser pulse with central wavelength of $\lambda = 800$ nm, duration of 45 fs, and energy of 0.8 J is fo-

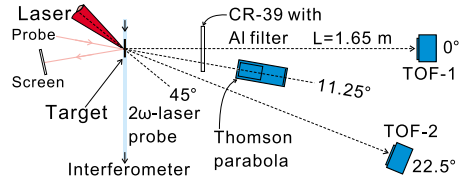

FIG. 1. (Color online) Experimental setup.

*Present address: High Energy Accelerator Research Organization (KEK), Japan.

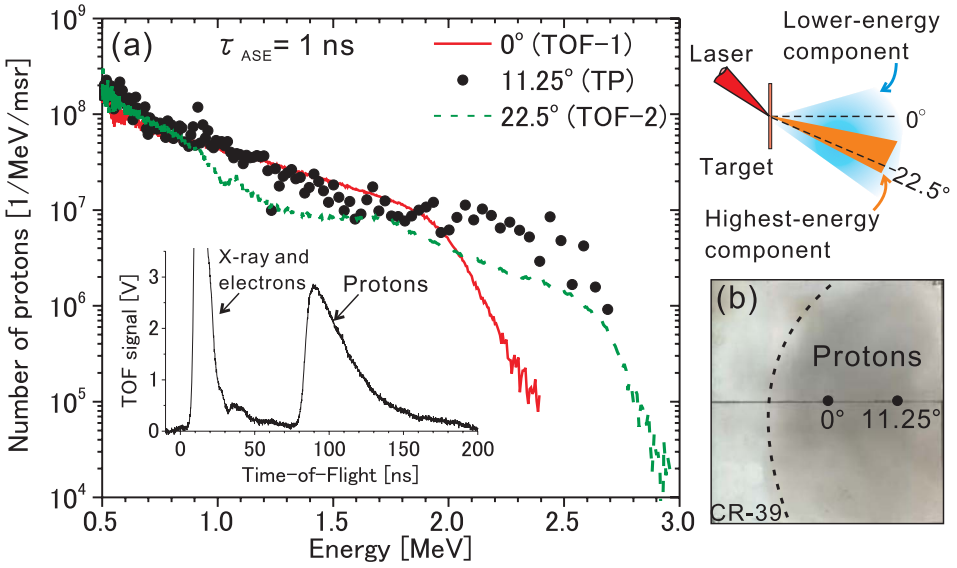

FIG. 2. (Color online) (a) Proton energy spectra simultaneously detected by TOF spectrometers, placed at 0° (solid line) and at 22.5° (dashed line) with respect to the target normal, and by the Thomson parabola (solid circles). The inset shows a typical TOF signal. (b) The spacial distribution of protons with energy above 1 MeV seen on the CR-39 film.

cused onto a 7.5-μm-thick polyimide $[(C_{22}H_{10}O_4N_2)_n]$ target at an incidence angle of 45° by a $f/3.5$ off-axis parabolic mirror. About 40% of the laser energy is contained in a $1/e^2$ focal spot with 10 μm diameter, giving a peak intensity of $I=1.5\times10^{19}$ W/cm^2. The fluctuations of the laser energy are within the 10% range, which is observed by a *p-i-n* photodiode detector which provides a trigger signal for the TOF analysis, [18]. The measured main-pulse—to—ASE intensity contrast ratio is 2.5×10^5 starting from 10 ps before the main pulse. The duration of the ASE pedestal is controlled by adjusting the Pockels cell in the range from 0.7 to 5 ns, monitored for each laser shot by a *p-i-n* photodiode detection system. The polyimide tape is continuously fed by a servomotor for each laser shot. The accuracy of positioning in the direction of the target normal, $\Delta x<15$ μm [19], is much smaller than the Rayleigh length (50 μm, in the same direction), provided by the parabolic mirror. Fluctuations of the target normal direction in the horizontal plane, not exceeding ±0.1°, are monitored during the experiment by the diode-laser probe shown in Fig. 1. The plasma cloud produced by the ASE pedestal is observed by the interferometer [20] using a probe beam with the wavelength of 400 nm. The plasma image is taken at the time of 50 ps before the main-pulse arrival.

Protons are measured by two online TOF spectrometers placed behind the target at the angles of 0° (TOF-1) and of 22.5° (TOF-2) with respect to the direction of the target normal, Fig. 1. Each TOF spectrometer is equipped with a plastic scintillator (PS), as a detecion medium, and a photomultiplier tube (PMT). Protons, generated in the laser-target interaction, arrive at the PS detector after passing a $L=1.65$ m tube. The PS signal is amplified by the PMT and displayed on an ocsilloscope as a TOF signal corresponding to a flight-time distribution of protons. A typical TOF signal is shown in the inset in Fig. 2(a). The TOF signal $V(t)$ (a function of time t) is used to calculate the proton energy spectrum $F(\mathcal{E})$ via the relation $V(t)dt=-C(\mathcal{E})F(\mathcal{E})d\mathcal{E}$, where $C(\mathcal{E})$ is the TOF detector efficiency depending on the proton kinetic energy, $\mathcal{E}\approx m_p v_p^2/2$. Here m_p and $v_p=L/t$ are the proton mass and velocity. The detection efficiency, $C(\mathcal{E})$, was calibrated using proton beams from a conventional accelerator [18]. In addition, the proton energy spectra are measured by the Thomson parabola (TP) ion analyzer equiped with the ion-track detector (CR-39) as a detection medium. The TP is placed in a bisector between the directions of the two TOF spectrometers (at the angle of 11.25°), Fig. 1. The spacial distribution of protons are also detected by another CR-39 plate covered with an aluminum filter mask.

III. RESULTS AND DISCUSSION

A. Effect of the ASE pedestal

Typical proton energy spectra are shown in Fig. 2(a) for the target normal (TOF-1: solid line) and for the 22.5° (TOF-2: dotted line) directions. As a reference, we show the spectrum recorded by the TP analyzer in the 11.25° direction (TP: circles). These three spectra are obtained simultaneously in a single laser shot, where the ASE duration is 1 ns. Protons emitted at angles of 11.25° and 22.5° have higher energy than those emitted in the target normal direction. We note that the energy resolution for 3 MeV protons is 0.2 MeV [18]. Figure 2(b) shows the spacial profile of the protons having energies above 1 MeV observed by the CR-39 detector covered with a 13-μm-thick aluminum filter. We see that the protons with higher energy are emitted at some angle between the target normal and the laser-propagation direction, so the fast proton beam direction turns out to be shifted from the target normal. In Ref. [7], similar shifts were considered as a result of a bending of the target rear surface caused by an ASE-generated shock wave. In our case, as shown below, the ASE causes a significant expansion of the target at its rear side, forming a gently sloping density profile, whose scale increases with the ASE duration τ_{ASE}, while the proton energy remains about the same level for 1 ns$<\tau_{ASE}<$3 ns.

The proton maximum energy $\mathcal{E}_{max}$ detected at the angles of 0° and of 22.5° with respect to the target normal is shown in Fig. 3(a) as a function of the ASE duration, τ_{ASE}. Two

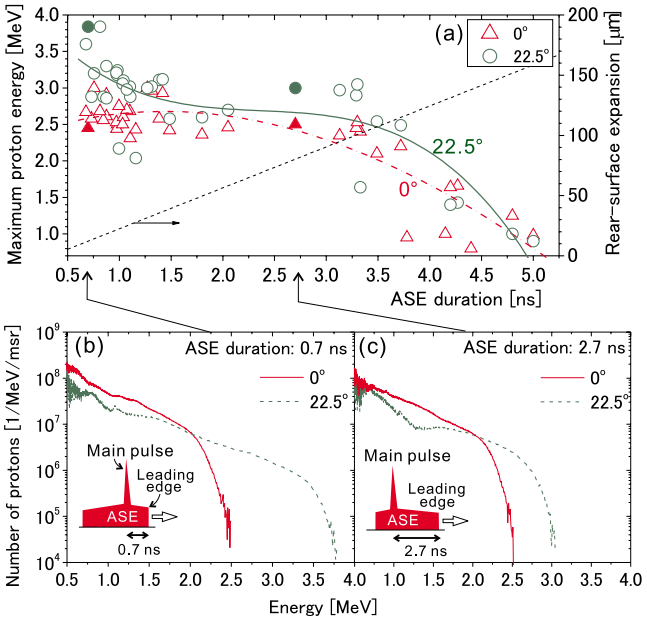

FIG. 3. (Color online) (a) The maximum proton energy $\mathcal{E}_{max}$ vs the ASE duration τ_{ASE}, as detected by TOF spectrometers at 0° (triangles) and at 22.5° (circles). Two curves are the analytical fits for $\mathcal{E}_{max}$ data points observed at 0° (dash-dotted line) and 22.5° (solid line) directions, respectively. The dashed line is for the thickness of plasma corona at the target rear side (see the text). The solid triangles and circles are for the TOF spectra detected with the ASE durations of τ_{ASE}=0.7 ns (b) and τ_{ASE}=2.7 ns (c).

curves are the analytical fits for $\mathcal{E}_{max}$ data points by third-order polynominal functions. One can see again that the proton energy is detected higher at the angle of 22.5° than the target normal (0°). Examples of the TOF spectra obtained for τ_{ASE}=0.7 and 2.7 are shown in frames 3(b) and 3(c), respectively. We note that τ_{ASE}=0.7 ns is the minimum achievable ASE duration in this experiment. The proton highest energy is 3.8 MeV, detected at the angle of 22.5°, Fig. 3(b). For protons with energy above 1 MeV, the laser-to-proton energy conversion efficiency is $f_{eff} \approx 0.3\%$.

The thickness of the plasma formed at the target rear side due to ASE can be estimated as follows. The ablation pressure p_a (expressed in TPa units) induced by a laser with an intensity of I_{ASE} (in terms of 10^{14} W/cm^2) and a wavelength of λ (measured in μm) is approximately equal to $p_a \simeq 0.86(I_{ASE}/\lambda)^{2/3}$ [21], independently of the target materials. In our case, the ASE pedestal with intensity $I_{ASE} \simeq 6 \times 10^{13}$ W/cm^2 produces an ablation pressure of $p_a \simeq 0.7$ Tpa, for which recent Hugoniot data [22] give estimations of a shock-wave velocity $v_s \simeq 22$ μm/ns and a particle velocity $v_p \simeq 17$ μm/ns, respectively. The shock wave reaches the rear surface of the 7.5-μm-thick polyimide target in $7.5/v_s \simeq 0.3$ ns, and the rear surface begins to move into vacuum with a velocity $2v_p \simeq 34$ μm/ns. Thus, during the time period of τ_{ASE} before the arrival of the main pulse, the rear surface is expanded to the distance $l_{ex}=2v_p(\tau_{ASE} - 7.5/v_s)$. This estimation is shown in Fig. 3(a) by the dashed line. A significant breakout of the rear surface occurs even for the shortest ASE duration in this measurement, τ_{ASE}

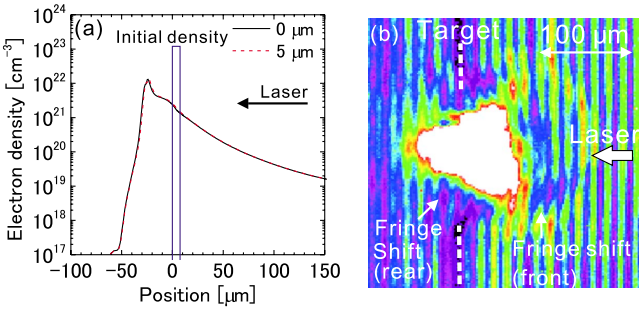

FIG. 4. (Color online) (a) The electron density profiles at initial time (rectangular profile) and after 1.5 ns on exposure to the ASE: at the ASE axis (solid line) and at a distance of 5 μm from that axis (dashed line), obtained in the 2D HD simulation. (b) The plasma image taken by the interferometer with the 400-nm probe 50 ps before the main pulse.

=0.7 ns. We emphasize that the proton energy above 2.5 MeV is detected even for a relatively large ASE duraion, 3 ns, in which case the ASE-irradiated region of the target is completely converted into a nearly underdense plasma. In Fig. 3(a), $\mathcal{E}_{max}$ in the 22.5° direction increases when τ_{ASE} decreases toward 0.7 ns. Then, one may expect that even shorter durations would lead to higher energies. However, we should notice that the proton highest energy is obtained at an angle of 22.5°. If the ASE duration is decreased further, beyond the minimum achievable 0.7 ns, the proton energy in the 22.5° direction will turn to decrease at some ASE duration. This is because a proton beam is directed along the target normal in the case of a solid-density target, which has been investigated in several experiments [1]. Hence, in the present work, *prepulse control* is to keep the ASE duration at an appropriate value, not to reduce it ultimately.

We performed 2D HD simulations of the evolution of our polyimide target irradiated by the ASE pedestal with the help of the PINOCO code [23]. The result is shown in Fig. 4(a) for the ASE pedestal duration τ_{ASE}=1.5 ns. The ASE is incident on the target at right angles; it has a Gaussian distribution in the transverse direction with the full width at half maximum (FWHM) waist of 10 μm. As seen from the electron density profiles along the target normal, the rear surface loses its steep gradient before the main laser pulse arrives. The electron density maximum is reduced to 10^{22} cm^{-3}, which is somewhat 2 times higher than the critical density $n_{cr}=\pi\gamma/r_e\lambda^2 \approx 4.9\times10^{21}$ cm^{-3}, where $\gamma=(1+a_0^2)^{1/2} \approx 2.82$ is the relativistic factor, a_0 is the dimensionless amplitude of the main laser pulse, $a_0=0.85(\lambda/1\ \mu m) \times[I/(10^{18}\ \mathrm{W\ cm^{-2}})]^{1/2}$, $r_e=e^2/m_ec^2$ is the classical electron radius, and λ=0.8 μm is the laser wavelength. The interferometry measurement is shown in Fig. 4(b). Although the second-harmonic radiation converted from the main laser pulse partially saturates the plasma image, we notice slight shifts of the fringes on the rear surface around the saturated region, which indicate the plasma density from 10^{18} to 10^{19} cm^{-3}, in agreement with the tails of the density profiles seen in the 2D HD simulation. This allows us to conclude that the detected proton acceleration occurred in a *near-critical* plasma cloud. Recalling Ref. [10], where

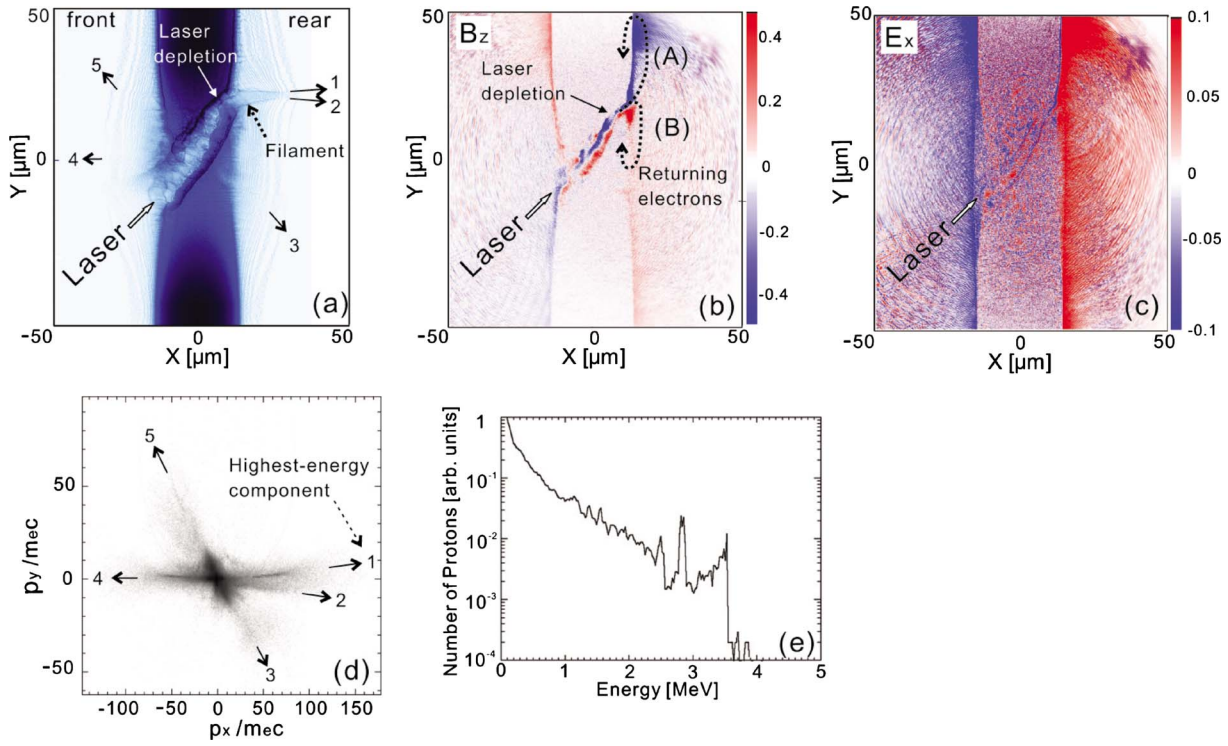

FIG. 5. (Color online) The 2D PIC simulation results. (a) The ion density after 300 laser periods from the laser pulse entrance. (b) The magnetic field B_z component and (c) the electric field E_x component, both normalized to $2\pi m_e c^2/e\lambda$, after 85 laser periods from the laser pulse entrance. (b) The ion phase-space projection onto the plane (p_x, p_y) after 300 laser periods from the laser pulse entrance. (e) The proton energy spectrum.

4 MeV proton acceleration from ultrathin (<100 nm) aluminum targets irradiated by a clean (ASE contrast $\approx 10^{10}$) 0.3-J, 33-fs, 10^{19}-W/cm^2 laser pulse with laser-to-proton energy conversion efficiency of about 1% was reported, we suppose that an optimal electron areal density [15] was achieved in both cases.

B. Acceleration mechanism

In order to reveal the mechanism of the proton acceleration in a near-critical plasma cloud, we performed 2D PIC simulations using the REMP code [24]. A *p*-polarized laser pulse with duration of 45 fs and intensity of 1.5×10^{19} W/cm^2 is focused at the 45° incidence angle onto a hydrogen plasma. Initially, the plasma cloud has a smooth distribution of the electron density (the target is assumed to be exploded by the ASE pedestal), ranging from $0.5n_{cr}$ to $2n_{cr}$ with a thickness of 24 μm in the direction of the x axis, which is normal to the initial target surface, Fig. 5. The (main) laser pulse goes into the near-critical density plasma, forming a long-living channel seen in the ion density distribution at the time of 300 laser periods after the laser pulse entrance, Fig. 5(a). Inside the channel, the ion density filament is formed [14]. The electrons accelerated along the laser pulse propagation direction, together with the return current of bulk electrons, form a long-living quasistatic magnetic field B, seen in Fig. 5(b). The electron vortices, associated with this magnetic field, move across the plasma density gradient, leave the channel, and spread over the target rear interface. At the rear side, the magnetic pressure induces and sustains a charge separation electrostatic field E, whose E_x component is shown in Fig. 5(c). This field accelerates ions [11,14]. The most important feature of the present mechanism is that the laser pulse is almost completely absorbed in the plasma slab. In Figs. 5(a) and 5(b), one can see that the laser pulse is depleted inside the target. The laser energy is efficiently converted into electron energy, resulting in the formation of the long-living magnetic field. Of course, the magnetic field can be induced also in the cases of low-density and solid-density targets. However, the near-critical plasma target provides better conditions for the laser pulse energy transformation into the fast electrons (a number of fast electrons is higher) and them into the magnetic field.

It should be emphasized that the quasistatic magnetic field is generated on the rear surface asymmetrically with respect to the target normal, as is seen in Fig. 5(b). Here, the magnetic field is induced more strongly in the region of (A) than (B). As a result, the electric field itself [Fig. 5(d)] is induced asymmetrically with respect to the target normal due to the magnetic field on the rear surface. This asymmetric acceleration field generates the proton beam shifted from the target normal direction. The ion phase plane (p_x, p_y) in Fig. 5(d), where p_x and p_y are the x and y components of the ion momentum, shows that the accelerated ions form five beamlets, whose directions are marked by arrows; the same directions are shown in the frame (a). The beamlets (1) and (2) correspond to ions accelerated in the forward direction, (4)—in the backward direction; beamlets (3) and (5) consist

of protons in the expanding channel walls. The highest-energy proton beamlet (1) is emitted at some angle between the target normal and the laser-propagation direction, in qualitative agreement with the experimental results. The proton energy spectrum in Fig. 5(e) exhibits a cutoff at an energy of 3.6 MeV, in agreement with the maximum energy observed in the experiment. The simulation shows that at the specified parameters the optimal conditions of the ion acceleration are met: a high absorption of the laser pulse, generation of a strong magnetic field, and formation of the ion density filament in the laser pulse channel.

The experimental and simulated results presented here indicate that the effect of the magnetic field should be taken into account in the acceleration mechanism. In the TNSA model [4], the electrostatic acceleration potential ϕ is proportional to the electron component pressure P_e via the relation $e\phi \propto P_e/n_e$, where n_e is the electron density. The magnetic field B will change this relationship into $e\phi \propto (P_e + B^2/8\pi)/n_e$, where the acceleration potential is improved by the magnetic field.

IV. CONCLUSION

In conclusion, we have demonstrated the laser-driven proton acceleration from a near-critical plasma cloud, which is modified by a duration-controlled ASE. The proton beam is directed at some angle away from the target normal. This is due to generation of the quasistatic magnetic field on the target rear side with the magnetic pressure inducing and sustaining a charge separation electrostatic field asymmetrically with the target normal. This fact implies that the effect of magnetic pressure should be introduced into the acceleration mechanism based on the hydrodynamical plasma expansion to vacuum. The acceleration mechanism discussed in this paper will be suitable in the future use of controllable target with optimal density [15]. Our results will pave a way for use of a new target which secures more controlled and stronger coupling with the laser pulse.

ACKNOWLEDGMENTS

This work is partly supported by the Ministry of Education, Culture, Sports, Science and Technology (MEXT) of Japan, Special Coordination Funds for Promoting Science and Technology (SCF), and a Grant-in-Aid for Young Scientists No. 18760659.

[1] M. Borghesi, J. Fuchs, S. V. Bulanov, A. J. Mackinnon, P. K. Patel, and M. Roth, Fusion Sci. Technol. **49**, 412 (2006).
[2] J. Fuchs, C. A. Cecchetti, M. Borghesi, T. Grismayer, E. d'Humiéres, P. Antici, S. Atzeni, P. Mora, A. Pipahl, L. Romagnani, A. Schiavi, Y. Sentoku, T. Toncian, P. Audebert, and O. Willi, Phys. Rev. Lett. **99**, 015002 (2007).
[3] T. Grismayer and P. Mora, Phys. Plasmas **13**, 032103 (2006).
[4] S. C. Wilks, A. B. Langdon, T. E. Cowan, M. Roth, M. Singh, S. Hatchett, M. H. Key, D. Pennington, A. MacKinnon, and R. A. Snavely, Phys. Plasmas **8**, 542 (2001).
[5] A. V. Gurevich, L. V. Pariiskaya, and L. P. Pitaevskii, Sov. Phys. JETP **22**, 449 (1966).
[6] A. J. Mackinnon, Y. Sentoku, P. K. Patel, D. W. Price, S. Hatchett, M. H. Key, C. Andersen, R. Snavely and R. R. Freeman, Phys. Rev. Lett. **88**, 215006 (2002).
[7] F. Lindau, O. Lundh, A. Persson, P. McKenna, K. Osvay, D. Batani, and C.-G. Wahlström, Phys. Rev. Lett. **95**, 175002 (2005).
[8] M. Kaluza, J. Schreiber, M. I. K. Santala, G. D. Tsakiris, K. Eidmann, J. Meyer-ter-Vehn and K. J. Witte, Phys. Rev. Lett. **93**, 045003 (2004).
[9] C. Thaury, F. Quéré, J.-P. Geindre, A. Levy, T. Ceccotti, P. Monot, M. Bougeard, F. Réau, P. d'Oliveira, P. Audebert, R. Marjoribanks, and Ph. Martin, Nat. Phys. **3**, 4241 (2007).
[10] D. Neely, P. Foster, A. Robinson, F. Lindau, O. Lundh, A. Persson, C.-G. Wahlström, and P. McKenna, Appl. Phys. Lett. **89**, 021502 (2006).
[11] K. Matsukado, T. Esirkepov, H. Daido, T. Utsumi, Z. Li, A. Fukumi, Y. Hayashi, S. Orimo, M. Nishiuchi, S. V. Bulanov, T. Tajima, A. Noda, Y. Iwashita, T. Shirai, T. Takeuchi, S. Nakamura, A. Yamazaki, M. Ikegami, T. Mihara, A. Morita, M. Uesaka, K. Yoshii, T. Watanabe, K. Kinoshita, T. Hosokai, A. Zhidkov, A. Ogata, Y. Wada, and T. Kubota, Phys. Rev. Lett. **91**, 215001 (2003).
[12] T. Utsumi, K. Matsukado, H. Daido, T. Z. Esirkepov, and S. V. Bulanov, Appl. Phys. A: Mater. Sci. Process. **79**, 1185 (2004).
[13] L. Willingale, S. P. D. Mangles, P. M. Nilson, R. J. Clarke, A. E. Dangor, M. C. Kaluza, S. Karsch, K. L. Lancaster, W. B. Mori, Z. Najmudin, J. Schreiber, A. G. R. Thomas, M. S. Wei, and K. Krushelnick, Phys. Rev. Lett. **96**, 245002 (2006); S. V. Bulanov and T. Z. Esirkepov, *ibid.* **98**, 049503 (2007); L. Willingale, S. P. D. Mangles, P. M. Nilson, R. J. Clarke, A. E. Dangor, M. C. Kaluza, S. Karsch, K. L. Lancaster, W. B. Mori, Z. Najmudin, J. Schreiber, A. G. R. Thomas, M. S. Wei, and K. Krushelnick, *ibid.* **98**, 049504 (2007).
[14] A. V. Kuznetsov, T. Z. Esirkepov, F. F. Kamenets, and S. V. Bulanov, Plasma Phys. Rep. **27**, 211 (2001); S. V. Bulanov, D. V. Dylov, T. Z. Esirkepov, F. F. Kamenets, and D. V. Sokolov, *ibid.* **31**, 369 (2005).
[15] T. Esirkepov, M. Yamagiwa, and T. Tajima, Phys. Rev. Lett. **96**, 105001 (2006).
[16] Y. Oishi, T. Nayuki, T. Fujii, Y. Takizawa, X. Wang, T. Yamazaki, K. Nemoto, T. Kayoiji, T. Sekiya, K. Horioka, Y. Okano, Y. Hironaka, K. G. Nakamura, K. Kondo, and A. A. Andreev, Phys. Plasmas **12**, 073102 (2005).
[17] T. Nayuki, Y. Oishi, T. Fujii, K. Takano, X. Wang, A. A. Andreev, K. Nemoto, and K. Ueda, J. Appl. Phys. **100**, 043111 (2006).
[18] S. Nakamura, Y. Iwashita, A. Noda, T. Shirai, H. Tongu, A. Fukumi, M. Kado, A. Yogo, M. Mori, S. Orimo, K. Ogura, A. Sagisaka, M. Nishiuchi, Y. Hayashi, Z. Li, H. Dadio, and Y. Wada, Jpn. J. Appl. Phys., Part 2 **45**, L913 (2006); A. Yogo, H. Daido, A. Fukumi, Z. Li, K. Ogura, A. Sagisaka, A. S. Pirozhkov, S. Nakamura, Y. Iwashita, T. Shirai, A. Noda, Y. Oishi, T.

Nayuki, T. Fujii, K. Nemoto, I. W. Choi, J. H. Sung, D.-K. Ko, J. Lee, M. Kaneda, A. Itoh, Phys. Plasmas **14**, 043104 (2007).

[19] T. Nayuki, Y. Oishi, T. Fujii, K. Nemoto, T. Kayoiji, Y. Okano, Y. Hironaka, K. G. Nakamura, K. Kondo, and K. Ueda, Rev. Sci. Instrum. **74**, 3293 (2003).

[20] A. Sagisaka, A. S. Pirozhkov, H. Daido, A. Fukumi, Z. Li, K. Ogura, A. Yogo, Y. Oishi, T. Nayuki, T. Fujii, K. Nemoto, S. Orimo, M. Nishiuchi, Y. Hayashi, M. Mori, M. Kado, S. Nakamura, A. Noda, I. W. Choi, J. H. Sung, D.-K. Ko, and J. Lee, Appl. Phys. B: Lasers Opt. **84**, 415 (2006).

[21] A. Benuzzi, T. Löwer, M. Koenig, B. Faral, D. Batani, D. Beretta, C. Danson, and D. Pepler, Phys. Rev. E **54**, 2162 (1996).

[22] K. Takamatsu, N. Ozaki, K. A. Tanaka, T. Ono, K. Nagai, M. Nakai, T. Watari, A. Sunahara, M. Nakano, T. Kataoka, H. Takenaka, M. Yoshida, K. Kondo, and T. Yamanaka, Phys. Rev. E **67**, 056406 (2003).

[23] H. Nagatomo, T. Johzaki, T. Nakamura, H. Sakagami, A. Sunahara, and K. Mima, Phys. Plasmas **14**, 056303 (2007).

[24] T. Zh. Esirkepov Comput. Phys. Commun. **135**, 144 (2001).